Enhanced water evaporation via coupled capillary transport and gelation in confined nanocrystal systems

Zengbin Wang,[1] Dan Xu,[1,2] Qun Song,[1] Siyuan Liu,[1] Xintong Meng,[1] Shaohuang Chen,[1,3] Philipp Vana,[4,5] and Kai Zhang[1,5,*]

[1]*Sustainable Materials and Chemistry, Department of Wood Technology and Wood-based Composites, University of Göttingen, Büsgenweg 4, D-37077 Göttingen, Germany*

[2]*Department of Material Chemistry, Graduate School of Engineering, Kyoto University, Kyoto 615–8510, Japan*

[3]*State Key Laboratory of Chemical Engineering, Tianjin Key Laboratory of Membrane Science and Desalination Technology, Collaborative Innovation Center of Chemical Science and Engineering (Tianjin), School of Chemical Engineering and Technology, Tianjin University, Tianjin 300072, China*

[4]*Institute of Physical Chemistry, University of Göttingen, Tammannstr. 6, D-37077 Göttingen, Germany*

[5]*Wöhler Research Institute for Sustainable Chemistry (WISCh), University of Göttingen, Tammannstr. 2, D-37077 Göttingen, Germany*

(Received 6 May 2025; accepted 18 September 2025; published 28 October 2025)

Drying in confined systems is a critical process with broad implications, spanning applications from materials science to water management in microscale technologies. Nevertheless, the coupled dynamics of transport and gelation in confined drying of colloidal suspensions remains poorly understood. Here cellulose nanocrystals (CNCs) are employed as a model system to systematically investigate the temporal dynamics, kinetic behavior, and structural transformation of nanocrystal suspensions during capillary drying. We report a mechanism whereby CNC suspensions, upon exceeding a critical concentration (∼1 wt%), undergo a transition from a fluid-like state to a kinetically arrested gel state at the evaporation front. This transition is accompanied by pinning of the evaporation interface at the capillary opening and leads to the formation of a gel–film heterostructure, consisting of a CNC gel layer with a water concentration gradient and a thin surface film formed via interfacial slip. This heterostructure promotes directional water transport from the capillary interior to the interface and significantly enhances the effective evaporative area, thereby accelerating the overall drying process. These findings offer insights into confinement-driven drying behavior and establish a framework for regulating evaporation kinetics in colloidal systems.

DOI: 10.1103/y5sn-g9vm

I. INTRODUCTION

Evaporation is a fundamental process with widespread significance in nature, daily life, and industry, driving the global water cycle, sustaining ecosystems, and enabling applications from food preservation to material production [1–3]. For dispersions containing suspended or colloidal particles, drying represents a prototypical nonequilibrium process, in which solvent evaporation drives a transition from a dilute phase to a concentrated phase [4,5]. This progression involves a complex interplay of mechanisms, including surface tension gradients, contact line pinning, Marangoni convection, and capillary flows arising from spatially heterogeneous evaporation [6,7]. Together these phenomena form a rich and dynamic landscape that has been extensively investigated at macroscopic scales [1,8,9], offering valuable experimental data and theoretical insights into drying processes [10]. In contrast, liquid evaporation in confined spaces presents far greater complexity due to significant influences from geometric constraints and interfacial effects [7]. These complexities manifest as nonuniform stress distribution, increased diffusion resistance, and imbalances in drying rates and structural shrinkage, all of which profoundly affect structure formation and drying efficiency [11].

In such confined systems, physical boundaries and geometrical constraints play a critical role in modulating transport phenomena and particle dynamics during evaporation [12,13]. These constraints can induce a shift from classical diffusion-limited regimes to more nuanced transport modes, such as molecular-scale fluxes near the Knudsen layer [14]. A broad range of microscale confinement configurations, such as spherical droplets [10], parallel-plate cells [15,16], Hele-Shaw geometries [17], and microfluidic channels [18], have been studied, demonstrating the profound influence of geometry on vapor diffusion, flow field organization, and particle spatial arrangement [19,20]. Notably, microscale confinement can drive distinct spatial organization and interfacial stratification of colloidal particles near boundaries, thereby modulating both flow behavior and drying kinetics [21]. A deeper understanding of these coupled physicochemical

*Contact author: kai.zhang@uni-goettingen.de

Published by the American Physical Society under the terms of the Creative Commons Attribution 4.0 International license. Further distribution of this work must maintain attribution to the author(s) and the published article's title, journal citation, and DOI.

processes is critical for the rational design of hierarchical materials. Despite these insights, most existing studies emphasize static outcomes [11,19], with limited attention to the real-time interactions among evaporation-driven transport, concentration-induced gelation, and evolving interfacial dynamics. In particular, the mechanisms by which these couplings regulate water delivery to the evaporating front and ultimately control drying kinetics remain insufficiently explored. The feedback loops among gel formation, flow restriction, and evaporation enhancement have rarely been systematically examined.

In this work we report a mechanism in which confined cellulose nanocrystal (CNC) suspensions exhibit coupled capillary transport and concentration-induced gelation, leading to significantly accelerated drying. *In situ* observations of the evaporation interface using polarized optical microscopy (POM) demonstrate that as water evaporates, CNC particles gradually accumulate at the solid-liquid-air three phase contact line. Rheological tests further confirm that the suspension transitions from a fluid-like state to a gel state, leading to the formation of the gel-film heterostructure at the capillary opening. Further analysis shows that the gel layer, which exhibits a concentration gradient, efficiently transports water from the interior of the capillary to the evaporation interface. Meanwhile, the thin film formed by residual CNCs via interfacial slip increases the effective evaporative surface area, thereby accelerating water evaporation. By adjusting the initial CNC concentration, the extent of interfacial slip can be modulated, allowing precise control over the evaporation rate. Moreover, the hydroxyl-rich surface chemistry of CNCs not only activates water molecules and lowers the evaporation enthalpy, further enhancing water evaporation, but also imparts selective affinity for water, enabling the preliminary concentration and separation of water from mixed solutions.

II. EXPERIMENTAL SECTIONS

Materials and chemicals

Microcrystalline cellulose (MCC), 2,2,6,6-tetramethylpipyridine-1-oxyl (TEMPO), sodium bromide (NaBr), and dimethyl sulfoxide (DMSO) were purchased from Sigma-Aldrich. Sulfuric acid (H_2SO_4, 98 wt%), periodic acid (HI_5O_6), Roth potassium hydroxide (KOH), and sodium hypochlorite (NaClO, 14 wt% a.q.) were purchased from VWR. Ethanol and *N,N*-dimethylformamide were purchased from Chemsolute. All chemicals were of analytical grade or higher. Deionized water (DI water) was used throughout the experiments.

III. METHODS

A. Preparation and purification of CNCs and ChNCs

CNCs were extracted from MCC via H_2SO_4 hydrolysis and designated as SCNCs. Briefly, MCC (10 g) was hydrolyzed in 200 ml of 65 wt% H_2SO_4 at 45 °C under continuous stirring for 45 min. Following hydrolysis, the reaction was quenched with approximately 600 ml of cold deionized water, and the suspension was subsequently washed and dialyzed. CNCs prepared via TEMPO-mediated oxidation, as described previously, were termed TO-CNCs [22], while those synthesized by periodic acid oxidation according to our prior method were referred to as PO-CNCs [23]. S-ChNCs [24] and PO-ChNCs [25] were prepared using the sulfuric acid hydrolysis method and the periodate oxidation method, respectively, following the procedures described in the literature. To ensure uniformity across all samples, CNC suspensions were purified and separated by centrifugation at 9000 rpm to yield homogenous CNC suspensions.

B. Capillary filling and drying procedure

Circular glass capillary tubes (Miniature Hollow Glass Tubing, Paul Marienfeld GmbH) with a fixed length of 80 mm were used in the experiments. The outer diameters were 0.6 mm, 0.8 mm, and 1.0 mm, and the corresponding inner diameters were 0.2 mm, 0.45 mm, and 0.8 mm, respectively. CNC suspensions at various concentrations were introduced into open-ended capillaries by immersing one end in the suspension for a few seconds, allowing partial filling to a set length. The capillary was then laid horizontally, and the evaporation of the liquid in the capillary was observed at ambient temperature. The birefringence evolution of the CNCs during drying was monitored by microscopy. Square capillaries (0.3 mm × 0.3 mm × 80 mm) were custommade for this study.

C. Water transport and separation experiment

After the CNC suspension formed a gel-film heterostructure as described above, water or a water mixture with DMSO or *N,N*-dimethylformamide was injected into the capillary tube via syringe from the opposite end to observe changes in the liquid residence length over time.

D. Simulation of water evaporation in capillary tubes

COMSOL Multiphysics® software was utilized to simulate the water evaporation in capillary tubes. The Stefan flow was considered. The geometric parameters were set according to those in the experiments. Further details can be found in the Supplemental Material [26].

E. Characterizations

1. Cross-polarized optical microscopy (POM)

POM measurements were conducted using a Nikon ECLIPSE E600 imaging microscope equipped with perpendicular polarizers and a Nikon DS-Fi2 camera for capillaries with inner diameters of 0.2 mm and 0.45 mm. Images of capillaries with a 0.8 mm inner diameter were obtained using a Leica S8AP0 microscope. All samples were placed on glass slides for observation under ambient conditions. POM was employed to monitor birefringence evolution in real time, with the capillary azimuthal angle set at 45° to maximize light intensity.

2. Scanning electron microscopy (SEM)

The scanning electron microscopy (SEM) images were obtained on a LEO Supra-35 High-Resolution Field Emission Scanning Electron Microscope (Carl Zeiss AG, Germany). The targeted voltage was 5 kV.

For surface imaging, after complete drying of the CNC suspension within the capillary, the capillary was immersed in liquid nitrogen to rapidly freeze the sample. The frozen capillary was then carefully fractured along its longitudinal axis using tweezers to expose the internal film at the open end. The sample was subsequently characterized on SEM.

For cross-sectional imaging, once the CNC suspension had fully dried inside the capillary, the resulting CNC gel was pushed out using a needle. The extracted gel was then frozen in liquid nitrogen. A blade was used to cut along the longitudinal axis to approximately halfway through the gel, and then the remaining part was gently broken off by rotating the blade. The exposed cross section was then imaged with SEM.

To image the pores within the gradient gel, a 2 wt% CNC suspension was allowed to dry inside a capillary tube. After 150 minutes drying, when a sufficiently long CNC gel was formed, the entire capillary containing the gel was rapidly frozen using liquid nitrogen to preserve its structure. The outer glass capillary was carefully fractured to extract the frozen CNC gel, which was subsequently freeze dried prior to SEM imaging.

3. Transmission electron microscopy (TEM)

The CNC samples were prepared from their aqueous suspensions of about 0.01 wt%. The transmission electron microscopy (TEM) observation was performed on a CM 12 Transmission Electron Microscope (Philips, the Netherlands).

4. Atomic force microscope (AFM)

Atomic force miscroscope (AFM) images were obtained through Atomic Force Microscope Bruker Multimode 8 (Bruker, Germany). The probes are SCANASYST-AIR-HR and SCANASYST-AIR.

For films on the inner surface of the capillary wall, after complete drying of the CNC suspensions inside the capillary, the entire capillary was rapidly frozen in liquid nitrogen to preserve its structure. The frozen capillary was then carefully fractured along the longitudinal axis using tweezers. The exposed sample was affixed onto an AFM sample stage to record the CNC alignment within the film.

For CNC alignment at the evaporation interface, once the CNC suspension was fully dried inside the capillary, the resulting CNC gel was extracted using a needle. The sample was then mounted on an AFM sample stage, and the alignment of CNCs at different regions of the evaporation front was characterized.

5. In situ polarized Raman microspectroscopy

Polarized Raman spectra were recorded using a LabRAM HR Evolution system (Horiba France SAS) with a 532 nm laser and an ND filter set to 10% transmission. Spectra were acquired with an exposure time of 20 sec, with each spectrum representing an accumulation of six scans. The estimated laser spot size was approximately 0.7 μm. Laser penetration depth varied depending on the sample, with a maximum estimated depth of 5–10 μm.

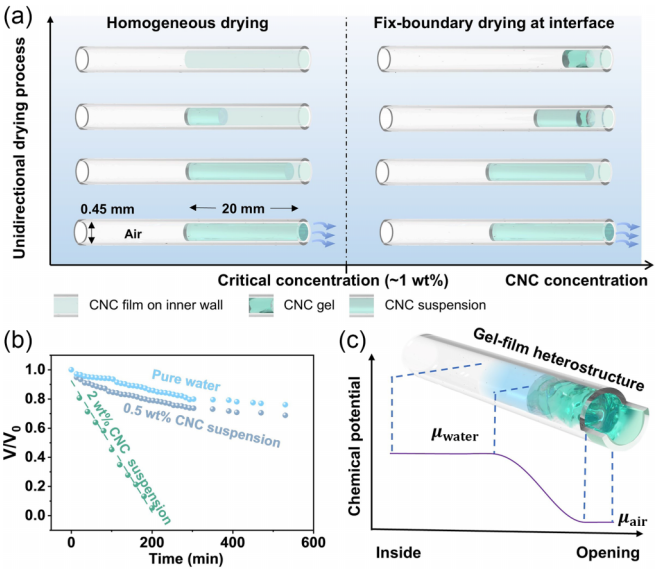


FIG. 1. Illustration of unidirectional drying of CNC suspension and the formation of gel-film heterostructures. (a) Two typical unidirectional drying processes of CNC suspensions. (b) Volume of the CNC suspensions of different concentrations and pure water in the capillary divided by the initial volume as a function of time. (c) Schematic illustration of the gel-film heterostructure at the fixed-boundary interface promoting water transport and evaporation.

6. Circular dichroism spectrum

Circular dichroism (CD) spectra were obtained using a JASCO J-1700 CD Spectrometer (JASCO Corporation, Japan) with a wavelength range of 190 to 790 nm. Signals for CD (mdeg), LD (mdeg), HT (V), and Abs were collected. After complete drying of the CNC suspension inside the capillary, the resulting CNC gel was extracted using a needle and placed at the center of the CD stage for testing.

7. Fourier-transform infrared spectroscopy (FTIR)

Attenuated total reflection Fourier-transform infrared spectroscopy was performed using an Alpha FT-IR Spectrometer (Bruker, Germany). The spectra were recorded at room temperature in the range of 4000–400 cm^{-1} as the average of 24 scans and a 4 cm^{-1} resolution.

8. Zeta potential

The zeta potential of aqueous suspensions containing CNC (approximately 0.5 mg/ml) and ChNC (approximately 0.5 mg/ml) was measured using a Nano-ZS instrument (Malvern Instruments Ltd., UK). Each sample underwent three measurements.

9. Rheological property

The rheological properties were measured using an HR 20 rheometer (TA Instruments, USA). A parallel plate with 20.00 mm diameter was applied and the distance of gap was set to 300 μm. The steady-state shear viscosity was measured across a shear rate range of 0.1–100 s^{-1}. To establish the linear viscoelastic region, a strain sweep was initially performed

with strains ranging from 1% to 100% at a constant angular frequency of 1 rad/s. The LVR was defined as the strain range in which the elastic modulus (G′) exhibited less than a 5% decrease from its initial value. Subsequently, rheological tests were conducted angular frequency ranges of 0.1–100 s^{-1} at room temperature. These measurements yielded the elastic modulus (G′) and loss modulus (G″), which together provide a comprehensive characterization of the sample's viscoelastic properties.

To investigate the potential phase transition behavior of CNCs during evaporation, time-dependent rheological measurements were performed. A 4 wt% CNC suspension was loaded between parallel plates with a 300 μm gap, and the test was conducted under a constant strain of 10%. By monitoring the temporal evolution of the storage modulus and loss modulus, the rheological response and phase behavior of the system during water evaporation were analyzed.

10. Differential scanning calorimetry (DSC)

Differential scanning calorimetry (DSC) scans were recorded on a NETZSCH DSC/200/F3 (NETZSCH, Germany) under a constant nitrogen flow (20 ml/min) with a heating/cooling rate of 5 K/min.

IV. RESULT

A. Unidirectional drying induces gel-film heterostructures

Following established methods in the literature, CNCs are prepared through sulfuric acid hydrolysis [27,28]. This process produces CNCs with an average length of 214 ± 41 nm, a diameter of 12 ± 3 nm, and an aspect ratio of 10 ± 4 (Supplemental Fig. 1 [26]). Due to the abundant sulfonate functional groups on their surface exhibiting a zeta potential of 53.26 mV (Supplemental Fig. 2 [26]), a stable and uniformly dispersed CNC suspension is obtained. The CNC suspension is drawn into a capillary tube with an inner diameter of 0.45 mm through capillary force, achieving a filling length of approximately 20 ± 3 mm in a capillary with a total length of 80 mm (Supplemental Fig. 3 [26]). The capillaries are subsequently placed horizontally under ambient conditions. Because of the long air column at the unfilled end, air circulation within the capillary is significantly restricted, resulting in minimal water vapor diffusion from this section. Thus, evaporation from this end is considered negligible. In contrast, at the filled end, where the suspension is directly exposed to the ambient air, evaporation primarily occurred due to the substantial chemical potential gradient. Therefore, the investigation focuses primarily on the evaporation process at the filled end.

The entire evaporation process is monitored in real-time under a microscope, allowing detailed observation of its dynamic behavior. It is observed that the initial CNC concentration has a significant influence on the evaporation process. When the CNC concentration exceeds 1 wt%, the evaporative interface initially recedes slightly before becoming pinned close to the capillary opening while the internal liquid column continues moving toward the opening until evaporation is complete (Fig. 1(a); Supplemental Fig. 4 [26]). During this process, CNCs deposit onto the capillary wall, forming a thin film, while simultaneously creating a CNC gel at the evaporation interface. Together, these components constitute a gel-film heterostructure (Supplemental Fig. 5 [26]) within the capillary. This entire process is completed within approximately 200 min, during which liquid water of the CNC suspension evaporates [Fig. 1(b)]. In contrast, when the CNC concentration is lower, e.g., 0.5 wt%, the evaporative interface does not remain pinned but gradually recedes inward until drying of CNC suspensions [Fig. 1(a); Supplemental Fig. 6 [26]] During this process, all CNCs deposit onto the capillary wall, forming a uniform thin film (Supplemental Fig. 7 [26]). The overall evaporation process takes more than 50 hr, with an evaporation rate comparable to that of pure water in the capillary [Fig. 1(b)]. Notably, the gel-film heterostructure exhibits remarkable stability. When pure water is introduced at the opposite end of the capillary, the gel layer efficiently absorbs water through capillary forces and chemical concentration gradients, transporting it to the interface, The water subsequently evaporates via the interface and film at the capillary wall [Fig. 1(c)].

B. Formation mechanism and process of gel-film heterostructures

Taking 2 wt% CNC suspension as a model system, the transition state of CNC suspensions within capillaries during water evaporation is investigated, aiming to elucidate the mechanism and processes underpinning the confined self-assembly of CNCs into gel-film heterostructures at the evaporative interface. COMSOL simulations (Supplemental Figs. 8, 9, and 10 [26]) indicate that the evaporation predominantly occurs at the three-phase boundary where the capillary wall, liquid and air converge. This localized evaporation preferentially facilitates the CNC accumulation in this region. We conducted *in situ* observations using POM during the first

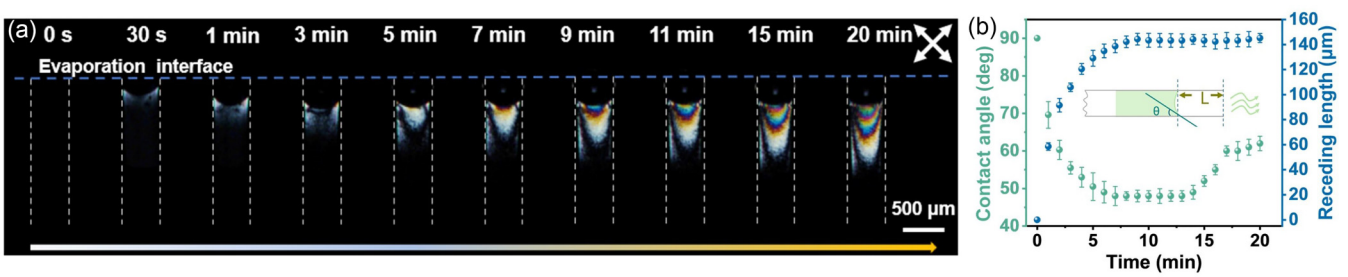


FIG. 2. Kinetics of the evaporation process. (a) Development of the evaporative interface during the first 20 min evaporation of the 2 wt% of CNC suspension in the capillary. (b) Variation of contact angle and evaporative interface retraction length over time for the first 20 min.

20 min of evaporation. Initially, when the CNC suspension was freshly introduced into the capillary, the liquid interface at the capillary opening remains flat [Fig. 2(a)]. At this stage, the random distribution of CNCs in the suspensions still does not generate birefringence under POM (Supplemental Fig. 11 [26]) . As evaporation progresses, a concave meniscus gradually forms at the evaporative interface due to capillary forces. Water evaporation was rapid at the three-phase contact line, so that CNCs accumulate in this region and pronounced birefringence emerges. With continued evaporation, the evaporative interface progressively "slips" inward along the capillary wall [29] [Figs. 2(a) and 2(b)], leaving behind a layer of CNC film on the capillary wall.

By the eighth minute, the evaporative interface becomes pinned and ceases to recede, and the contact angle reaches a minimum [Fig. 2(b)], marking a critical point where the CNC concentration at the interface reaches a threshold. At this stage, the cohesive forces between CNCs effectively counterbalance the adhesive forces exerted by the capillary wall [30]. As evaporation continues, the CNC concentration at the interface further increases, accompanied by visible birefringence and color changes. Driven by the chemical concentration gradient, CNC suspension within the capillary is continually transported from the capillary interior toward the evaporative interface, leading to the gradual formation of a gel layer. Due to the abundant hydroxyl/sulfate groups on the CNC surface, this gel layer acts as a medium for water transport, facilitating the continuous delivery of water from the capillary interior to the evaporative interface to maintain chemical concentration equilibrium. Notably, a slight increase in the contact angle is observed by the 16th minute [Figs. 2(a) and 2(b)], which is attributed to further dehydration of CNCs gel and enhanced hydrogen bonding between CNCs, causing a minor contraction at the interface.

Therefore, during the drying process of CNC suspensions in capillary, the suspension gradually transitions from a liquid state to a kinetically arrested gel state. Here it is proposed that the observed "pinning" effect results from the balanced cohesive forces within the CNC gel layer and the adhesive forces between CNC and the capillary wall. As water evaporates, CNC concentration near the evaporation interface steadily increases, driving the suspension towards kinetic arrest, which in turn enhances cohesive force and results in a stationary evaporation interface. Our investigation of the concentration dependence of CNC suspensions reveals that increasing CNC concentration reduces surface tension (Supplemental Fig. 12 [26]) while simultaneously enhancing cohesive energy. Additionally, the yield stress of CNC suspension increases with rising concentration, indicating stronger flow resistance at the orifice at higher concentrations [Fig. 3(a)]. The CNC suspension gradually transitions into a gel state, which macroscopically manifests as a slowing of the interface retraction rate [Figs. 2(a) and 2(b)]. Subsequently, we investigated the rheological behavior of CNC suspensions across varying concentrations. The results show that the viscosity of CNC suspensions decreases with increasing shear rate over the entire measured shear rate range [Fig. 3(b)]. At low CNC concentrations, the viscosity-shear rate curve reveals two distinct regimes: at low shear rates, the viscosity changes may be associated with variations in the disclination lines within the

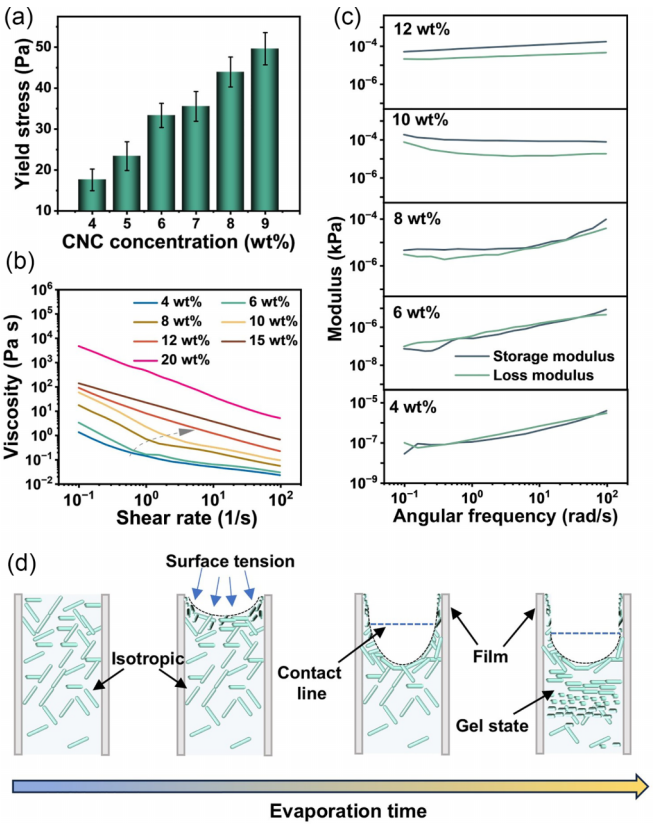


FIG. 3. Characterization of rheological properties. (a) The relationship between yield stress and concentration of CNC suspensions. (b) The relationship between viscosity and concentration of CNC suspensions. (c) The frequency sweep curves of CNC suspensions. (d) A schematic illustration of the mechanism of CNC self-assembly in the region of evaporative interface due to surface tension/evaporation-induced stress. The contact line is defined as the locus where the gas-liquid interface meets the capillary wall, observed macroscopically as the apparent intersection between the meniscus and the capillary wall.

polydomain texture, whereas the viscosity increase is likely related to nanocrystal alignment along the flow direction at high shear rates (in a regime with a lower slope than the first) [31]. As CNC concentration further increases, this transition point shifts toward higher shear rates, indicating enhanced flowability of the solution with higher concentration. The rheological properties of CNC suspensions demonstrate that, as the CNC concentration increases, the storage modulus gradually exceeds the loss modulus, indicating a more pronounced solid-like gel behavior [Fig. 3(c); Supplemental Fig. 13 [26]].

Hence, we propose that the drying process of CNC suspension within a capillary can be divided into three distinct stages [Fig. 3(d)]. Initially, during the early evaporation phase, the CNC concentration is relatively low, and the cohesive force is insufficient to counteract deformation driven by the surface tension at the glass surface, resulting in slippage and a concave meniscus at the interface. As evaporation progresses, the CNC concentration gradually increases, resulting in higher CNC concentration at the interface. This eventually leads to a kinetically arrested stage with steadily increasing cohesive force and yield stress, accompanied by a reduction in the

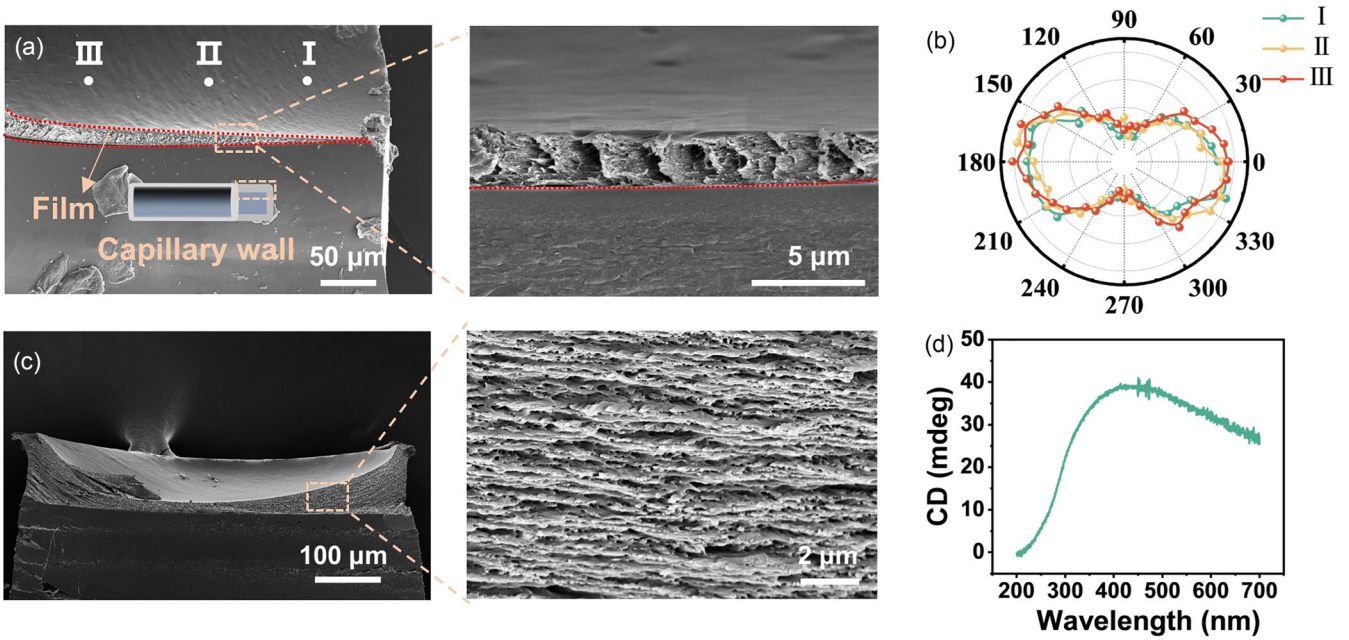


FIG. 4. Structural characterization of gel-film heterostructures. (a) SEM image of the CNC film on the capillary wall. (b) CNC alignment characterized by polarized Raman spectroscopy. (c) SEM image of the cross section at the evaporation interface of the CNC film, formed after drying the gel layer, which was obtained through brittle fracturing of the sample in liquid nitrogen. (d) Circular dichroism (CD) spectrum of cross section of the film formed after drying of the CNC gel layer.

liquid-solid interfacial tension near the capillary wall. When the cohesive force and surface tension reach a critical threshold, the CNC interface becomes "pinned" and remains stable. As water continues to evaporate at the evaporation interface, CNCs accumulate layer by layer at the surface, gradually forming a gel layer. The evaporation of water within the gel induces a significant capillary pressure at the interface, ultimately leading to the formation of a CNC gel with a distinct concentration gradient structure (Supplemental Fig. 14 [26]).

The formation of the gel-film heterostructure is significantly influenced by key parameters, such as initial CNC concentration and capillary diameter. For a given capillary diameter, the initial CNC concentration determines the duration of kinetic arrest during the drying process, thus affecting the distance from the capillary opening at which pinning occurs (Supplemental Fig. 15 [26]), but this does not impact the subsequent CNC gel formed during kinetic arrest (Supplemental Table 1 [26]). When the CNC concentration exceeds 5%, the high concentration leads to a rapid increase in concentration upon water evaporation, resulting in a stationary evaporation interface and direct gel layer formation at the capillary opening.

In addition to concentration, capillary diameter plays a critical role in structure formation (Supplemental Fig. 16 [26]). A larger capillary diameter requires a higher CNC yield stress, resulting in a higher concentration at the pinning point. If the yield stress does not reach the threshold, the interface continues to recede until evaporation is complete, and no gel structure is formed in this process.

C. Morphology and structure analysis

We next investigated the structures formed during the evaporation process. After fracturing the capillary along its longitudinal axis, strong interactions between CNCs and the capillary wall during slippage induce the adhesion of CNCs, forming a CNC layer. After complete drying, a progressively thicker CNC film was observed on the capillary wall [Fig. 4(a)]. Interestingly, the CNC film exhibited a chiral helical structure, which may facilitate water transport [32]. To further analyze CNC alignment, we employed *in situ* Raman spectroscopy taking measurements at the front, middle, and rear sections of the film [Fig. 4(b)]. The results revealed that CNCs were aligned perpendicular to the longitudinal axis of the capillary across all regions. This alignment was likely induced by surface tension torque acting during the receding of the liquid interface [33,34] while orienting surface CNCs perpendicularly to the long axis (Supplemental Fig. 17 [26]). AFM results confirmed the Raman measurements (Supplemental Fig. 18 [26]), providing evidence for the perpendicular alignment of CNCs in the film.

To investigate the structure at the evaporation interface, CNC suspensions were introduced into 0.8 mm capillaries to a length of approximately 5 mm, allowing for the formation of a thin gel layer, followed by drying under ambient conditions. During this process, the kinetically arrested gel layer gradually lost water contracting to form a thin film while preserving the CNC alignment. POM revealed that the resulting film exhibited a clear radial topological structure with a distinct Maltese cross pattern [Supplemental Fig. 19(a) [26]]. This pattern indicates a symmetrical arrangement of CNC. In the POM-λ images, with a λ plate providing a 530 nm retardation, alternating yellow and blue regions were observed within the Maltese cross pattern [Supplemental Fig. 19(b) [26]], suggesting that CNCs may be arranged tangentially along the evaporation interface [35]. To further confirm CNC arrangement at the evaporation interface, *in situ* polarized Raman

spectroscopy was performed at different positions along the film. The results showed that CNCs in the peripheral regions of the evaporation interface were tangentially aligned along the circumference (Supplemental Fig. 20, regions I, II, III, and IV [26]), with the alignment gradually diminishing toward the center (Supplemental Fig. 20, regions III and V [26]), In contrast, CNCs in the central region are randomly oriented (Supplemental Fig. 20, region VI [26]). AFM results corroborated these *in situ* Raman observations, providing additional evidence for the alignment pattern observed at the evaporation interface.

We propose that the initial alignment of CNC primarily occurs at the three-phase interface, with Brownian motion and surface tension acting as key factors governing CNC orientation. In the absence of external forces, the Brownian motion of CNCs allows them to rotate and translate freely, resulting in a random structure. Once an external force becomes dominant, the behavior of CNCs at the three-phase contact line deviates significantly from that observed in the bulk suspension. As CNCs are transported with water molecules toward the three-phase contact line, one end of the CNC is fixed to the contact line. At this juncture, surface tension generates a torque that acts to minimize the interfacial free energy. This torque directs the CNCs, gradually aligning them parallel to the evaporative interface (Supplemental Figs. 17 and 21 [26]). Concurrently, water evaporation at the three-phase interface induces a migration of water from the capillary center toward the capillary walls, further promoting CNC alignment. This alignment effect diminishes progressively from the capillary edge toward the center. In comparison, opposing directional flows cancel each other, leading to a random arrangement of CNCs at the capillary center (Supplemental Fig. 20 [26]). This spatial gradient in alignment highlights the interplay between surface tension torque and evaporative flows in structuring CNC alignment.

Cross-sectional analysis of the dried CNC gel at the interface showed that CNCs are internally arranged in layers and exhibit a left-handed helical structure [Fig. 4(c)]. This is similar to CNC films formed via evaporation-induced assembly in Petri dishes [28,36]. Circular dichroism (CD) further verifies the presence of a chiral structure with a absorption peak maximum of approximately 423 nm [Fig. 4(d)].

D. Enhanced water transport and evaporation via gel-film heterostructures

When the CNC concentration exceeds the critical threshold, the evaporation interface becomes pinned at the capillary opening, which helps stabilize the location of the evaporative front and facilitates continuous liquid transport from the interior of the capillary. At this interface, the liquid molecules are in direct contact with the external air, enabling rapid evaporation of liquid from the capillary. Interestingly, CNC suspensions of different initial concentrations exhibit varying water evaporation rates within the capillary, with a concentration of 2 wt% achieving the highest evaporation rate [Fig. 5(a)]. We hypothesize that this phenomenon arises from the differing pinning positions of CNC at varying initial concentrations, which results in films of different lengths along the capillary walls (Supplemental Fig. 15 [26]). FTIR analysis

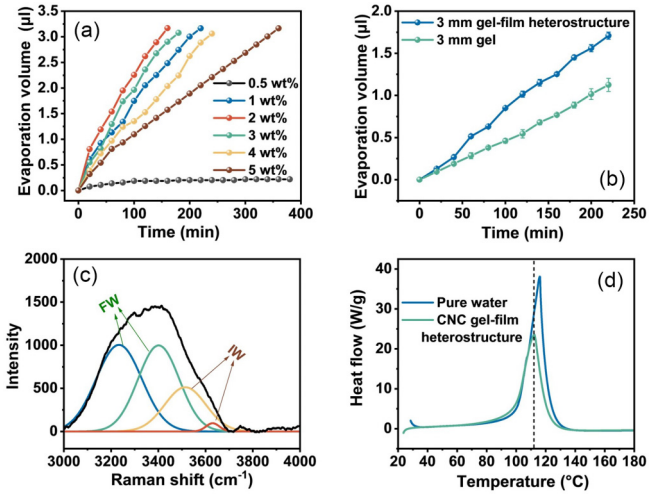


FIG. 5. Gel-film heterostructures enhance water transport and evaporation. (a) Evaporation time of a 20 mm CNC liquid column (0.32 μl) with different initial concentrations in 0.45 mm capillary. (b) The amount of water evaporated over time from CNC gel-film heterostructures and CNC gel within a 0.45 mm capillary. (c) Raman spectra showing the fitting peaks representing IW and FW in the CNC gel-film heterostructure. (d) DSC curves of the CNC gel-film heterostructure and pure water.

revealed that the film region retained a relatively high water content during evaporation, indicating that the presence of the film increased the effective evaporative surface area and thereby accelerated water evaporation (Supplemental Fig. 22 [26]). However, excessively long films can hinder the water transport through the film, and the increased distance between the pinned interface and the capillary opening ultimately lowers the evaporation rate. At CNC concentration of 2 wt%, the film length and receding distance are optimally balanced, resulting in a faster evaporation rate under ambient conditions.

To evaluate the functional role of the gel-film heterostructure in water evaporation, we conducted control experiments by filling capillaries with CNC gel of the same concentration. The results showed that the evaporation rate of the evaporation-induced CNC gel-film heterostructure is significantly higher than that of standard CNC gel [Fig. 5(b)], demonstrating that the film actively promotes water evaporation.

To further elucidate the role of CNC in enhancing the water evaporation, we investigated the activation of water by CNC and categorized the water molecules within the gel network into three types based on hydrogen bonding: free water (FW), intermediate water (IW), and bound water (BW) (Supplemental Fig. 23 [26]). Raman spectral analysis of the O-H stretching region revealed distinct water types within the CNC gel-film heterostructure. Peak fitting analysis revealed that peaks at 3233 cm^{-1} and 3401 cm^{-1} correspond to free water with four hydrogen bonds-two protons and two lone electron pairs engaging in hydrogen bonding with neighboring water molecules. In contrast, peaks at 3514 cm^{-1} and 3630 cm^{-1} are attributed to intermediate water with weaker hydrogen bonds [37]. Notably, intermediate water constituted approximately 19% of the water content in the CNC gel-film heterostructure

[Fig. 5(c)], effectively lowering the total energy required for water transport and evaporation.

Differential scanning calorimetry (DSC) analysis further corroborated these findings and indicated that the peak evaporation temperature for CNC gel is lower than that of pure water, suggesting more readily volatilized water in CNC gel. Additionally, the CNC gel displayed a broader half-width and a lower peak intensity compared to pure water, suggesting the coexistence of significant amounts of IW and BW alongside FW. These distinct water types evaporate progressively with increasing temperature, resulting in a smoother and broader evaporation peak [Fig. 5(d)].

Notably, once the CNC gel-film is formed, it can continuously transport water from the interior of the capillary to the evaporation interface (Supplemental Fig. 24 [26]), highlighting its potential for handling water in slits. Furthermore, the abundance of hydroxyl/sulfate groups on the CNC surface provides high selectivity for water in mixed solutions. When 3.7 μl of a water-DMSO mixture solution is introduced into the capillary, water preferentially evaporated through the CNC gel under ambient conditions (Supplemental Fig. 25 [26]), leaving behind DMSO. Analysis of solutions with varying water-DMSO ratios reveals rapid initial evaporation of water. However, as the water content decreases, the remaining water molecules engage in stronger intermolecular interactions with DMSO that significantly reduces water volatility [38]. This process further suppresses water evaporation, ultimately preventing complete separation of water and DMSO under ambient conditions. Beyond DMSO, the CNC gel-film heterostructure demonstrated effective water separation from other water-miscible solvents (Supplemental Fig. 26 [26]), underscoring its broader potential applications for selective water removal across various solvent systems.

Notably, the formation of a gel-film heterostructure at the evaporation front for accelerated water transport and evaporation is not limited to SCNC suspensions. CNC and ChNC suspensions with various surface functionalities including carboxylated CNCs via TEMPO-mediated oxidation (TO-CNCs), periodate-oxidized CNCs (PO-CNCs), and ChNCs with distinct functional groups, such as periodate-oxidized ChNCs (PO-ChNCs) and sulfuric acid hydrolyzed ChNCs with sulfonic acid groups on surface (S-ChNCs) (Supplemental Fig. 27 [26]), were further investigated. The results demonstrate that, upon reaching a critical concentration, these suspensions also form gel-film layers at the evaporation front as water evaporates. These layers function as conduits, continuously directing water from the interior of the capillary to the evaporation front, significantly enhancing the evaporation rate (Supplemental Fig. 28 [26]). To explore the applicability of this phenomenon in capillaries with diverse geometries, the drying behavior in rectangular capillaries was also examined. The experimental results revealed that the drying process in rectangular capillaries mirrors that in circular capillaries (Supplemental Fig. 29 [26]), with gel-film layer formation similarly accelerating internal water evaporation.

V. CONCLUSION

In summary, our study demonstrates that compared to pure water or low concentration CNC suspensions, higher concentration CNC suspensions facilitate the coupling of capillary transport and interfacial gelation, leading to the formation of a gel-film heterostructure that significantly enhances water evaporation efficiency. Through POM observations and rheological testing, we investigated the dynamic behavior of the evaporation process. Initially, as water evaporates, the evaporation interface gradually recedes into the capillary, forming a CNC film along the inner capillary wall, while the CNC concentration at the interface steadily increases. When the suspension's cohesive energy exceeds the adhesive force exerted by the capillary, the evaporation interface becomes pinned. Subsequently, the suspension within the capillary flows toward the evaporation interface, forming a CNC gel. This gel acts as a transport medium, efficiently delivering water from the capillary interior to the evaporation interface, further accelerating water evaporation. Additionally, the hydroxyl-rich surface of CNCs lowers the evaporation enthalpy of water, further enhancing evaporation efficiency. The gel-film heterostructure exhibits excellent stability, continuously transferring water from the capillary interior to the interface for evaporation. Finally, we validated the generality of this phenomenon using other nanocrystals and rectangular capillaries. This study provides insights into water management and control in microsystems.

ACKNOWLEDGMENTS

K.Z. thanks the EU for financially supporting the project "NEuM" (ZW7-85191973) and the German Research Foundation (DFG) and the Lower Saxony Ministry of Science and Culture for the project INST186/1397–1/FUGG. Z.W., Q.S., S.L., X. M., and S.C. thank China Scholarship Council (CSC) for the financial support of their Ph.D. study.

K.Z. conceived the concept and supervised the project. Z.W. and K.Z. designed the experiments. Z.W. prepared all specimens and performed characterization. D.X. performed the COMSOL simulation. S.L. Q.S., and X.M. performed SEM, circular dichroism, and AFM experiments, respectively. All authors analyzed the results. Z.W. and K.Z. drafted the manuscript. All authors contributed to the discussion of results and writing and revision of the manuscript.

The authors declare no conflict of interest.

DATA AVAILABILITY

The data that support the findings of this article are not publicly available because they contain commercially sensitive information. The data are available from the authors upon reasonable request.

[1] R. D. Deegan, O. Bakajin, T. F. Dupont, G. Huber, S. R. Nagel, and T. A. Witten, Capillary flow as the cause of ring stains from dried liquid drops, Nature (London) **389**, 827 (1997).

[2] F. Clément and J. Leng, Evaporation of liquids and solutions in confined geometry, Langmuir **20** 6538 (2004).

[3] U. Thiele, Patterned deposition at moving contact lines, Adv. Colloid Interface Sci. **206**, 399 (2014).

[4] L. Daubersies and J.-B. Salmon, Evaporation of solutions and colloidal dispersions in confined droplets, Phys. Rev. E **84** 031406 (2011).

[5] D. Brutin and V. Starov, Recent advances in droplet wetting and evaporation, Chem. Soc. Rev. **47** 558 (2018).

[6] M. Cavallaro Jr., L. Botto, E. P. Lewandowski, M. Wang, and K. J. Stebe, Curvature-driven capillary migration and assembly of rod-like particles, Proc. Natl. Acad. Sci. USA **108** 20923 (2011).

[7] S. K. Wilson and H.-M. D'Ambrosio, Evaporation of sessile droplets, Annu. Rev. Fluid Mech. **55** 481 (2023).

[8] B. Pathak, S. Hatte, and S. Basu, Evaporation dynamics of mixed-nanocolloidal sessile droplets, Langmuir **33** 14123 (2017).

[9] I. G. Hwang, J. Y. Kim, and B. M. Weon, Droplet evaporation with complexity of evaporation modes, Appl. Phys. Lett. **110**, 031602 (2017).

[10] P. J. Yunker, T. Still, M. A. Lohr, and A. Yodh, Suppression of the coffee-ring effect by shape-dependent capillary interactions, Nature (London) **476** 308 (2011).

[11] Y. Lin, E. Balizan, L. A. Lee, Z. Niu, and Q. Wang, Self-assembly of rodlike bio-nanoparticles in capillary tubes, Angew. Chem. Int. Ed. **49** 868 (2010).

[12] R. D. Deegan, O. Bakajin, T. F. Dupont, G. Huber, S. R. Nagel, and T. A. Witten, Contact line deposits in an evaporating drop, Phys. Rev. E **62** 756 (2000).

[13] P. Gurrala, S. Balusamy, S. Banerjee, and K. C. Sahu, A review on the evaporation dynamics of sessile drops of binary mixtures: Challenges and opportunities, Fluid Dyn. Mater. Process. **17** 253 (2021).

[14] E. Bird and Z. Liang, Transport phenomena in the Knudsen layer near an evaporating surface, Phys. Rev. E **100** 043108 (2019).

[15] G. Chen, On paradoxical phenomena during evaporation and condensation between two parallel plates, J. Chem. Phys. **159**, 151101 (2023).

[16] R. Mondal and M. G. Basavaraj, Patterning of colloids into spirals via confined drying, Soft Matter **16** 3753 (2020).

[17] R. A. Lopez de la Cruz, N. Schilder, X. Zhang, and D. Lohse, Phase separation of an evaporating ternary solution in a Hele-Shaw cell, Langmuir **37** 10450 (2021).

[18] P. Bacchin, J. Leng, and J.-B. Salmon, Microfluidic evaporation, pervaporation, and osmosis: From passive pumping to solute concentration, Chem. Rev. **122** 6938 (2021).

[19] V. Cherpak, V. Korolovych, R. Geryak, T. Turiv, D. Nepal, J. Kelly, T. Bunning, O. Lavrentovich, W. Heller, and V. Tsukruk, Robust chiral organization of cellulose nanocrystals in capillary confinement, Nano Lett. **18** 6770 (2018).

[20] P. Liu, J. Wang, H. Qi, T. Koddenberg, D. Xu, S. Liu, and K. Zhang, Biomimetic confined self-assembly of chitin nanocrystals, Nano Today **43**, 101420 (2022).

[21] W. Liu, J. Midya, M. Kappl, H.-J. Butt, and A. Nikoubashman, Segregation in drying binary colloidal droplets, ACS Nano **13** 4972 (2019).

[22] T. Saito and A. Isogai, TEMPO-mediated oxidation of native cellulose. The effect of oxidation conditions on chemical and crystal structures of the water-insoluble fractions, Biomacromolecules **5**, 1983 (2004).

[23] P. Liu, B. Pang, S. Dechert, X. C. Zhang, L. B. Andreas, S. Fischer, F. Meyer, and K. Zhang, Structure selectivity of alkaline periodate oxidation on lignocellulose for facile isolation of cellulose nanocrystals, Angew. Chem. Int. Ed. **59** 3218 (2020).

[24] J. D. Goodrich and W. T. Winter, α-Chitin nanocrystals prepared from shrimp shells and their specific surface area measurement, Biomacromolecules **8** 252 (2007).

[25] P. Liu, H. Liu, T. Schäfer, T. Gutmann, H. Gibhardt, H. Qi, L. Tian, X. C. Zhang, G. Buntkowsky, and K. Zhang, Unexpected selective alkaline periodate oxidation of chitin for the isolation of chitin nanocrystals, Green Chem. **23** 745 (2021).

[26] See Supplemental Material at http://link.aps.org/supplemental/10.1103/y5sn-g9vm for further explanation of the simulation, additional experimental data, detailed derivations of theoretical results, and several illustrative figures.

[27] S. Mukherjee and H. Woods, X-ray and electron microscope studies of the degradation of cellulose by sulphuric acid, Biochim. Biophys. Acta **10**, 499 (1953).

[28] Q. Song, Z. Wang, D. Xu, S. Liu, H. Liu, and K. Zhang, Self-assembly of polysaccharide nanocrystals: From aggregation in suspensions to optical materials, Prog. Polym. Sci. **148**, 101768 (2024).

[29] E. Dussan, On the spreading of liquids on solid surfaces: Static and dynamic contact lines, Annu. Rev. Fluid Mech. **11** 371 (1979).

[30] D. Xu, X. Meng, S. Liu, J. Poisson, P. Vana, and K. Zhang, Dehydration regulates structural reorganization of dynamic hydrogels, Nat. Commun. **15** 6886 (2024).

[31] E. E. Ureña-Benavides, G. Ao, V. A. Davis, and C. L. Kitchens, Rheology and phase behavior of lyotropic cellulose nanocrystal suspensions, Macromolecules **44** 8990 (2011).

[32] Y. Liu, J. Zhang, and P. Wu, Near-frictionless long-distance water transport in trees enabled by hierarchically helical molecular pumps, CCS Chem. **7**, 484 (2025).

[33] M. Mashkour, T. Kimura, F. Kimura, M. Mashkour, and M. Tajvidi, Tunable self-assembly of cellulose nanowhiskers and polyvinyl alcohol chains induced by surface tension torque, Biomacromolecules **15** 60 (2014).

[34] M. Mashkour, T. Kimura, M. Mashkour, F. Kimura, and M. Tajvidi, Printing birefringent figures by surface tension-directed self-assembly of a cellulose nanocrystal/polymer ink components, ACS Appl. Mater. Interfaces **11** 1538 (2018).

[35] R. M. Parker, G. Guidetti, C. A. Williams, T. Zhao, A. Narkevicius, S. Vignolini, and B. Frka-Petesic, The self-assembly of cellulose nanocrystals: Hierarchical design of visual appearance, Adv. Mater. **30** 1704477 (2018).

[36] P.-X. Wang, W. Y. Hamad, and M. J. MacLachlan, Structure and transformation of tactoids in cellulose nanocrystal suspensions, Nat. Commun. **7** 11515 (2016).

[37] X. Zhou, F. Zhao, Y. Guo, B. Rosenberger, and G. Yu, Architecting highly hydratable polymer networks to tune the water state for solar water purification, Sci. Adv. **5** eaaw5484 (2019).

[38] K. I. Oh, K. Rajesh, J. F. Stanton, and C. R. Baiz, Quantifying hydrogen-bond populations in dimethyl sulfoxide/water mixtures, Angew. Chem. **129** 11533 (2017).